A Study on the potential industrial effluent remediation applications of CdS nanoparticles through niobium incorporation

Haewon Byeon[1], Priyanshu Kumar Singh[2], N. Shalom[3], M. Sivaprakash[4], Prakash A[5], D. Prince Sahaya Sudherson[6] and Sunil J[7*]

[1]Workcare D-Health Lab, Convergence Department, Korea University of Technology and Education (Korea Tech), Republic of Korea
[2]Department of Mechanical Engineering, Mepco Schlenk Engineering College, Sivakasi, Tamil Nadu, India
[3]Department of Mechanical Engineering, Noorul Islam Centre for Higher Education, Kumaracoil, India,
[4]Department of Mechanical Engineering, Stella Mary's College Engineering, Aruthenganvilai, Tamil Nadu, India
[5]Vel Tech Rangarajan Dr. Sagunthala R&D Institute of Science and Technology, Chennai, India.
[6]Department of Mechanical Engineering, Rohini College of Engineering & Technology, Palkulam, Tamil Nadu, India.
[7]Department of Mechanical Engineering, Annai Vailankanni College of Engineering, Kanyakumari, India.

*to whom all correspondence should be addressed: e-mail: sunil0520@gmail.com

Graphical Abstract

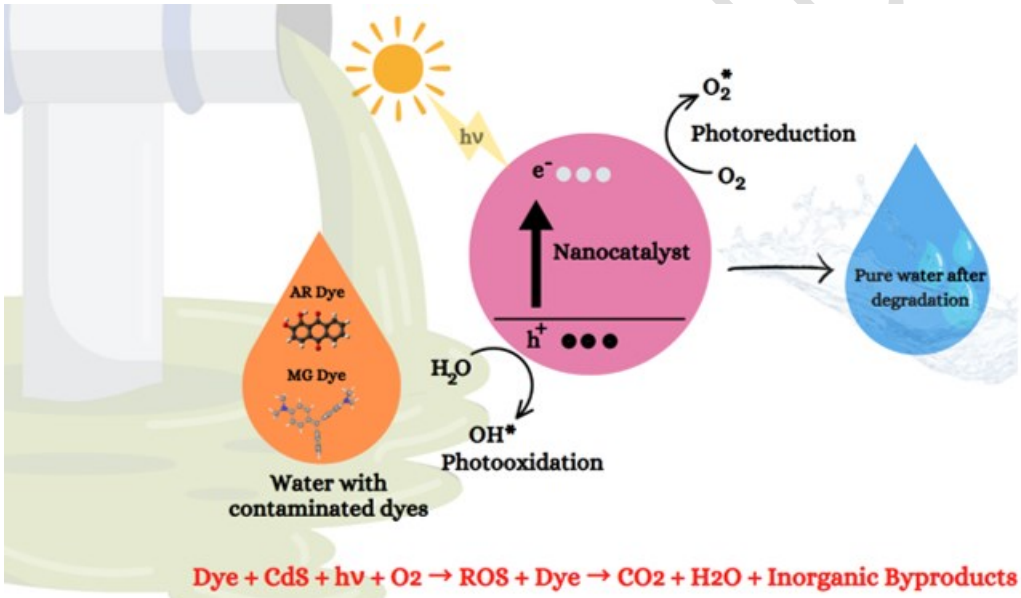

Abstract

The increasing release of textile dyes into water bodies poses a significant environmental challenge due to their toxicity and resistance to degradation. In this study, cadmium sulfide (CdS) nanoparticles (NPs) and niobium (Nb)-doped CdS at three different concentrations were synthesized using a green synthesis approach, employing *Syzygium cumini* seed extracts as eco-friendly reducing and capping agents. The results confirmed the formation of a wurtzite hexagonal phase, with decreasing crystal size. However, as the crystal size decreased, the bandgap increased to 2.60 eV due to the quantum confinement effect. The FE-SEM analysis revealed distinct morphologies influenced by Nb doping levels and EDAX confirms the sample purity. Photocatalytic studies under visible light demonstrated significant dye degradation for both Alizarin Red and Malachite Green. CdS-N_3 exhibited the highest kinetic rate constants of

2.03 and 2.32×10^{-2} min^{-1} for Alizarin Red and Malachite Green, respectively, with degradation efficiencies of 84.97% and 88.76%. Furthermore, Nb doping enhanced the stability, with CdS-N_3 maintaining 79.9% and 84.1% degradation efficiency after five cycles for Alizarin Red and Malachite Green, respectively. Additionally, NPs shown significant antibacterial activity against gram-positive bacteria, highlighting their potential for dual-function environmental remediation. The synergistic effects of Nb doping were found to enhance both photocatalytic degradation and antibacterial performance, making these materials promising candidates for sustainable wastewater treatment and microbial control.

Keywords: wastewater treatment; textile industry; aquatic ecosystems; Dye degradation; Antibacterial; Antioxidant

1. Introduction

The rapid expansion of the textile industry has significantly contributed to water pollution due to the discharge of toxic dye effluents. These dyes are often non-biodegradable, carcinogenic, and harmful to aquatic ecosystems. Conventional wastewater treatment methods, such as adsorption, chemical oxidation, and filtration, are either inefficient, energy-intensive or generate secondary pollutants. This creates an urgent need for sustainable, efficient, and eco-friendly solutions to address textile wastewater pollution (Jain *et al.* 2021). Semiconductor-based photocatalysis has emerged as a promising technology for degrading organic pollutants in wastewater. Among the many semiconductor materials, CdS NPs have a direct band gap of approximately 2.4 eV, which falls in the visible-light spectrum. This property allows it to efficiently bind solar energy, making it highly effective for visible-light-driven photocatalysis. It exhibits strong absorption in the visible region due to its optimal band gap, which enhances its light-harvesting capability (Nasir *et al.* 2020). This is crucial for applications like textile dye degradation, where visible-light activation is required. However, CdS faces challenges such as photo corrosion, limited charge carrier separation, and reduced stability. To enhance the performance of CdS NPs, doping with transition metals like Nb has shown potential which acts as an electron trap due to its higher oxidation state (Nb^{5+}). This traps photogenerated electrons, thereby reducing recombination and prolonging the lifetime of charge carriers and the enhanced charge separation boosts photocatalytic activity (Nunes *et al.* 2020). Moreover, Niobium has an ionic radius (Nb^{5+}: 0.64 Å) compatible with the CdS lattice, allowing it to integrate effectively without causing excessive distortion. The Nb is relatively non-toxic and poses minimal environmental risks, making it suitable for applications like water treatment and antibacterial use. Therefore, Nb doping transforms CdS NPs into a more efficient and multifunctional material, hence, is an optimal choice for doping CdS NPs due to its ability to enhance visible-light absorption, improve charge carrier dynamics, reduce photo corrosion, and boost antibacterial activity, all while maintaining compatibility with the CdS lattice. Consequently, the growing demand for environmentally friendly and sustainable processes has spurred interest in the green synthesis of NPs. Conventional synthesis methods often involve hazardous chemicals and energy-intensive processes, which raise environmental and safety concerns. To address this, the use of plant-based extracts as reducing and stabilizing agents has emerged as an eco-friendly alternative (Cui *et al.* 2022). *Syzygium cumini*, commonly known as jamun or black plum, is a tropical fruit tree with seeds rich in bioactive compounds, such as

polyphenols, flavonoids, and tannins, which facilitate the green synthesis of NPs. These natural compounds act as reducing and capping agents, enabling the formation of CdS NPs in a sustainable and non-toxic manner. These seeds are often discarded as waste after consuming the fruit. Utilizing seeds for green synthesis provides an eco-friendly way to upcycle agricultural byproducts, contributing to waste management and sustainability (Adeyemi *et al.* 2022). Thus, the current study focuses on the green synthesis of CdS NPs using *Syzygium cumini* (Jamun) seed extract, a natural source of bioactive compounds. These NPs are further doped with niobium with different concentrations to enhance their photocatalytic and antibacterial properties. Further by analyzing the structural, morphological, optical, and electronic properties via characterization techniques. The developed material is evaluated for its ability to degrade toxic textile dyes under visible light breaking down complex dye molecules into non-toxic byproducts assessing the antibacterial activity against certain pathogens and further addressing the dual challenges in wastewater treatment and public health.

2. Experimental Procedure

2.1 Materials used

Cadmium chloride ($CdCl_2$) and sodium sulfide (Na_2S) were used as the reactant materials, Niobium oxide (Nb_2O_5) as a dopant, double distilled water as a solvent, *Syzygium cumini* seed extract was added as the reducing and stabilizing agent and Hydrochloric acid to dissolve Nb_2O_5. This study made use of analytical chemicals sourced from Merck, India. They were used promptly without enduring any further purifying processes. *Escherichia coli* (ATCC 9677) gram-negative strain and *Staphylococcus aureus* (ATCC 6538P) gram-positive strains, Nutrient broth and Mueller Hinton agar (MHA) are processed by HiMedia in India.

2.2 Extract preparation

Initially, the seeds are removed from the pulp (jamun fruit), and thoroughly washing the seeds with running water to remove any residual fruit pulp, dirt, or impurities. Later, allow the seeds to air dry in the shade for 3–5 days to remove surface moisture and avoid direct sunlight, as it may degrade bioactive compounds. Once dried, crush the seeds into a coarse powder using a domestic grinder. Further, 20g of seed powder was added to 200 ml of DD water, and heating the mixture at 60–80°C for 60 minutes with constant stirring. This process helps extract bioactive compounds, such as tannins, polyphenols, and flavonoids, which are crucial for reducing and stabilizing NPs. Further allowing the solution to cool to room temperature. Then, filtering the cooled mixture using a Whatman filter paper to remove insoluble residues. Later, collecting the clear filtrate (aqueous seed extract) in a clean container. Moreover, the aqueous seed extract plays multiple roles in the green synthesis of NPs. The phytochemicals in the extract act as capping agents, preventing the aggregation of NPs which stabilizes the NPs and ensures uniform size and shape (Shabaani *et al.* 2020).

2.3 CdS-Nb NP synthesis

The CdS NPs were synthesized through a simple green synthesis method. First, separate aqueous solutions of cadmium precursor (0.5 M of $CdCl_2$) and sulfur source (0.5 M of Na_2S) were prepared by adding 100 ml of seed extract in the cadmium precursor solution under

constant stirring. This initiates the reduction of Cd^{2+} ions. Further, slowly add the sulfur source solution to the reaction mixture. Upon mixing, the reaction mixture undergoes a noticeable color change from light pale orange-yellow to bright yellow, and the NPs are formed as the reaction progresses (Adeyemi *et al.* 2022).

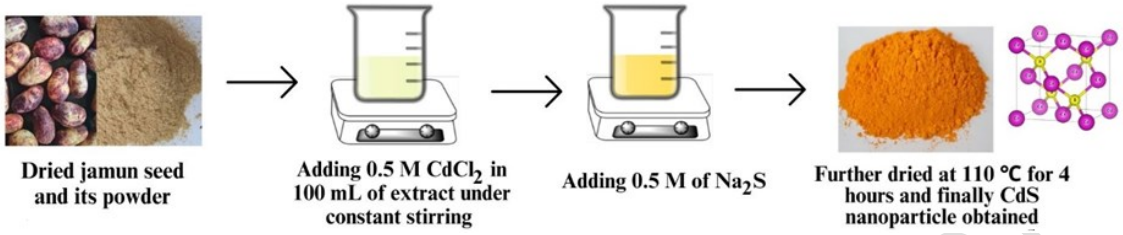

Figure 1. CdS NPs synthesis

The extract stabilizes the NPs during this process. Later, the reaction mixture was centrifuged to collect the synthesized particles followed by ethanol and DD water to eliminate impurities and further dried at 110℃ for 4 hours to obtain NPs. Since, Nb_2O_5 is insoluble in water, initially we need to be converted into soluble Nb species using HCl, and this forms niobium ions (Nb^{5+}). For doping Nb, it follows the above-mentioned synthesis process, after the addition of extract, the prepared Nb^{5+} solution (1%, 2%, and 3%) was dropwise added to the $CdCl_2$ mixture at different concentrations and stirred continuously to ensure the uniform distribution of Nb ions in the solution (Nunes *et al.* 2020). Later, the sulfur solution to the reaction mixture under constant stirring to promote the formation of Nb-doped CdS NPs (Abdel-Aty *et al.* 2021).

2.4 Antioxidant activity

The DPPH test assesses the capability of synthesized NPs to eliminate free radicals. Various concentrations (25, 50, 75 and 100 mg/mL) of NPs were used to examine their impact on antioxidant actions. Control solution (CS) represents the Pure DPPH, whereas Test solution (TS) denote the prepared CdS NPs and CdS-Nb. Using methanol as the blank, the absorbance at 518 nm was measured using a UV-visible spectrum. The evaluation of DPPH scavenging activity was conducted through the calculation of the percentage using a formula (Dravie *et al.* 2020);

$$\text{DPPH scavenging (\%)} = \frac{\text{CS}-\text{TS}}{\text{CS}} \text{ X } 100\ \% \quad (1)$$

2.5 Antibacterial activity

The bactericidal efficacy against gram-positive and -negative bacterial cultures, as well as the antibacterial standard Chlortetracycline (CT 30 mcg), was assessed using the well-diffusion method. The collection of cultured bacteria was added into Nutrient broth and incubated at a temperature of 36°C for 12 hours. Thereafter, carefully cultivated bacterial cultures were employed to extract specimens from the MHA medium and were subjected to a 12-hour incubation period. The previously mentioned colonies exhibited a significant inoculation within the solidified agar media contained in a Petri dish and these wells were filled with NPs at concentrations of 25, 50, and 100 mg/mL. Later, all the plates were subjected to incubation at 36℃ for a duration of 24 hours to facilitate the proliferation of bacteria within the medium

(Abdel-Aty *et al.* 2021). The measurement of the diameter of the growth inhibition was assessed in relation to the conventional standard agent.

2.6 Dye degradation process

The photocatalytic activity of the created NPs was assessed using model dyes: Alizarin red and Malachite green. The dye solution was created by dissolving the dye at a concentration of 20 mg/L (20 ppm) in separate beakers. Following this, 100 mL of each dye solutions underwent irradiation without the presence of a nano-catalyst, and its breakdown was evaluated using UV–Visible spectrum. Concurrently, 100 mg of NPs were each combined with 100 mL of dye solution (100 mg/L) and exposed to direct sunshine for 90 minutes, with 15 minutes intermissions. Thereafter, the UV–visible spectrum was systematically recorded, and the dye's decolorization was evaluated according to its optical absorption intensity. The effectiveness of dye degradation may be determined using the succeeding formula (Kong *et al.* 2022):

$$\eta = \frac{Co-Ct}{Co} X\ 100\% \quad (2)$$

where, η is degradation effectiveness, and Ct and Co are the final and initial concentrations of the prepared dye solutions.

2.7 Characterization techniques

A detailed study was performed on the physico-chemical characteristics of NPs created using biosynthesis, utilizing the following approaches. The UV–visible spectra spanning from 200 to 800 nm were obtained utilizing an Agilent (8085) UV–visible spectrophotometer. The determination of the bandgap of the NPs was achieved through the application of a Tauc relation plot. The surface morphology was examined utilizing FE-SEM.

3. Results and Discussion

3.1 Structural characterization

The presence of different diffraction peaks with broad peak exhibits a semi-crystalline nature of the synthesized CdS NPs and represented in Figure 2. They correspond to the wurtzite hexagonal phase of CdS as evidenced by the indexed planes, 25.1(100), 26.6(002), 28.6(101), 44.08(110), 48.12(103), 52.2(112) and match well with those in the JCPDS Card no. 41-1049. However, the broader and less intense peaks reflect semi-crystallinity. The Nb doping disrupts the periodic arrangement of the CdS lattice, introducing structural defects or disorder, leading to the observed semicrystalline nature (Abd *et al.* 2021). As the dopant concentration increases, the peaks become broader, indicating reduced crystallite size. Moreover, the intensity of peaks decreases slightly with higher Nb concentrations, indicating a reduction in crystalline order due to dopant-induced defects.

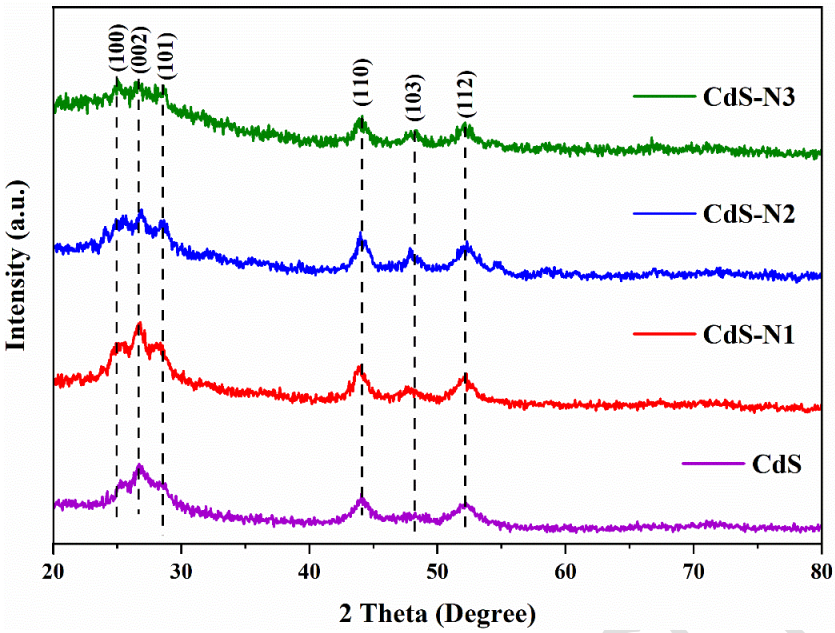

Figure 2. XRD spectra of synthesized NP

To calculate the crystal size and dislocation density from the given 2θ values, we need to apply the Debye-Scherrer equation for crystal size and a standard formula for dislocation density. The average crystal size is calculated to be 24.9, 19.09, 15.4, and 21.5 nm, respectively for CdS NP, CdS-N1, CdS-N2, and CdS-N3. The Nb have different ionic radii compared to Cd ions. When Nb is doped into the CdS lattice, it causes lattice distortion and generates strain, which hinders crystal growth (Yi *et al.* 2021). Furthermore, the plant extract acts as a natural stabilizer and growth inhibitor, reducing the crystal size by capping and enhancing nucleation. At higher concentrations, Ostwald ripening can dominate. Smaller particles dissolve, and larger particles grow as the system tries to minimize its total surface energy. Moreover, higher dopant concentrations may lead to agglomeration of smaller crystallites. These aggregates can fuse, forming larger crystals (Wang *et al.* 2007). The estimated structural parameters are shown in Table 1.

Table 1. Structural parameters of the synthesized NPs

Sample	Crystal size (nm)	Bandgap (eV)	Dislocation density 'δ' ($\times 10^{15}$ lines/m^{2})	Microstrain 'ε' ($\times 10^{-3}$ / lines^{2}m^{4})
CdS	24.9	2.41	0.002602	0.0402
CdS-N1	19.09	2.50	0.00678	0.0524
CdS-N2	15.4	2.60	0.00408	0.0649
CdS-N3	21.5	2.46	0.00376	0.0465

3.2 Morphology analysis

The FE-SEM images of prepared CdS NPs and CdS-Nb (CdS-N1, CdS-N2, CdS-N3) with different Nb doping levels (1%, 2%, and 3%) have been shown in Figure 3. The NPs (a) display a uniform size distribution, indicating controlled nucleation and growth during synthesis. A

smooth and consistent surface texture is visible, suggesting a lack of defects or structural irregularities. This indicates effective stabilization during synthesis. Further, minor agglomeration observed in certain areas is evident, potentially due to the biological components in the capping agents from the *Syzygium cumini* seed extract. The image (b) likely shows small, well-dispersed NPs with relatively uniform sizes. Low doping levels (1%) ensure minimal interference with the nucleation and growth of CdS NPs, leading to a morphology that remains close to pure CdS. The particles appear to have a smooth surface with slight agglomeration. This is expected, as the low Nb concentration introduces minimal structural distortions while retaining the intrinsic properties of CdS NPs. The FESEM image for CdS-N2 has been displayed in Figure (c). it reveals the petal-shaped morphology, where it exhibits thin, elongated, or layered structures that radiate or overlap like flower petals. At 2% Nb doping, the lattice distortions and changes in surface energy can promote directional growth, leading to the formation of petal-like structures. Moreover, the organic molecules might also influence the aggregation pattern, promoting petal-like arrangements. The morphology (Figure d) of CdS NPs doped with 3% Nb likely shows noticeable changes compared to lower doping levels due to the higher concentration of Nb and it exhibits rod-shaped morphology. Higher Nb doping concentrations (3%) can promote anisotropic growth, where certain crystal facets grow more rapidly than others. This directional growth leads to the formation of rod-like structures (Ali *et al.* 2017). The extract also facilitates the reduction process and stabilizes the NPsurface, giving the rods a refined texture.

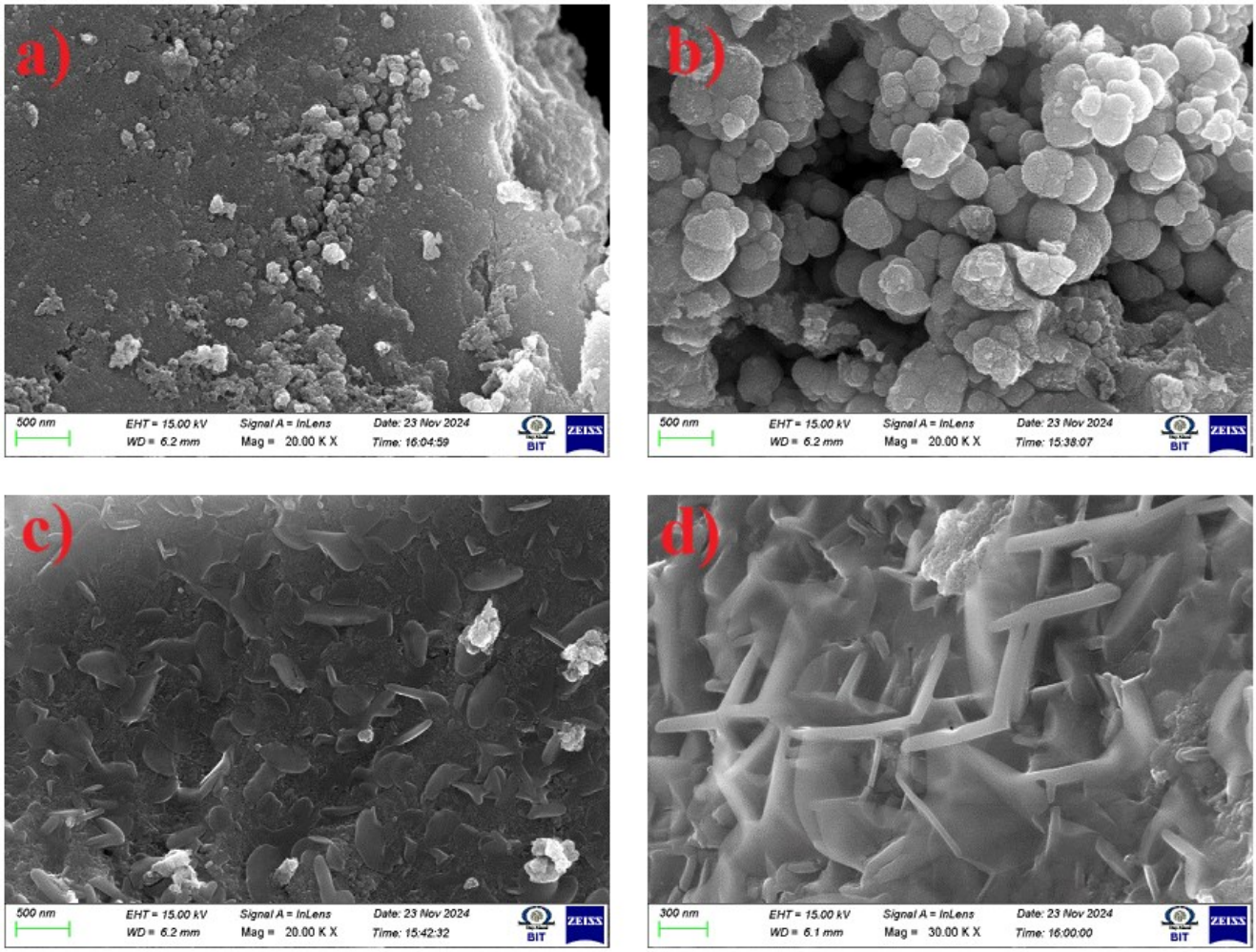

Figure 3. FE-SEM images of prepared (a) CdS, (b) CdS-N1, (c) CdS-N2, (d) CdS-N3 NPs

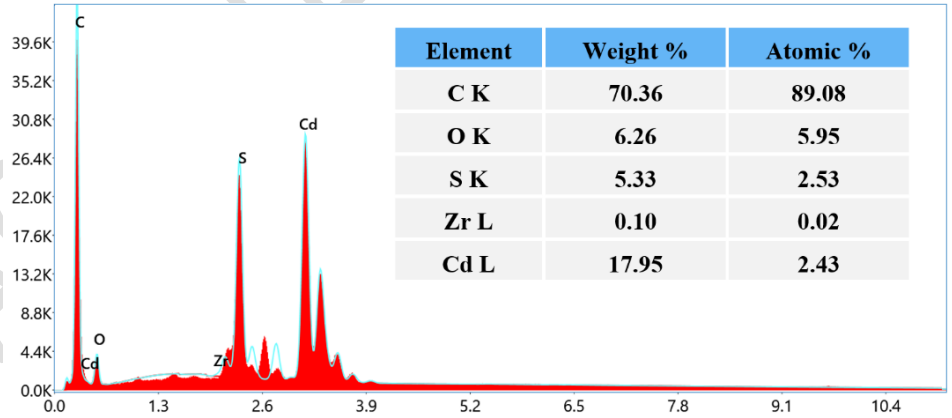

Element	Weight %	Atomic %
C K	70.36	89.08
O K	6.26	5.95
S K	5.33	2.53
Zr L	0.10	0.02
Cd L	17.95	2.43

Figure 4. EDX analysis of CdS-N3 NPs

The image (Figure 4) provided represents the EDX spectrum and quantitative analysis of CdS NPs with Nb and the presence of key elements confirming the successful synthesis of CdS NPs with organic surface functionality. The high percentage of carbon (70.36 wt.%) could be attributed to organic residues or capping/stabilizing agents and these agents often have a carbon-based structure and remain on the surface of the NPs. Oxygen (6.26 wt.%) likely

originates from hydroxyl/carboxyl groups present in the extract, indicating surface functionalization. Sulfur (5.33 wt.%) is a key element in CdS and its detection confirms the formation of the sulfide component of the material. Zirconium (0.10 wt %) presence in such a small amount might be due to trace contamination during synthesis and alternatively, it could be introduced through reagents used during the doping or functionalization process. Cadmium (17.97 wt.%) is the primary metal in the CdS material. Its presence confirms the successful incorporation of cadmium ions in the crystalline structure.

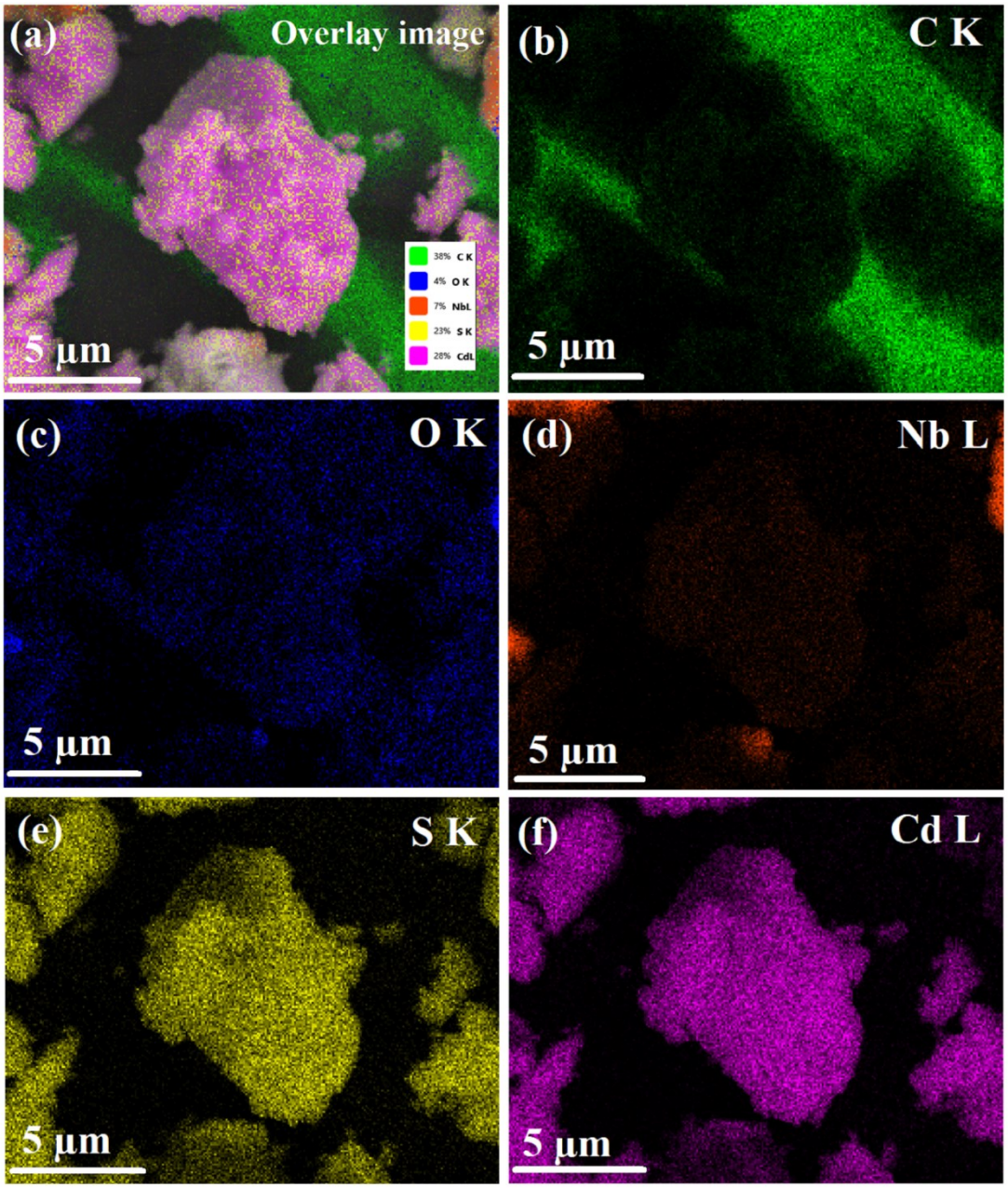

Figure 5. Elemental mapping of CdS-Nb3 NPs

The elemental mapping confirms the successful synthesis of Nb-doped CdS NPs with a reasonably uniform distribution of Cd, S, and Nb. From the image 5, a green color appears in dispersed regions, likely originating from residual organic compounds in the *Syzygium cumini* extract used in the synthesis. Blue color represents the Oxygen, representing either Nb_2O_5

remnants or adsorbed oxygen on the particle surface. The red color represents Nb, indicating the dopant's distribution across the CdS NPs. Where the yellow color represents Sulfur, a core element in the CdS structure. Pink color represents Cadmium, forming the main framework of the CdS NPs. The elemental mapping confirms the CdS-Nb NPs' structure, where Nb is well-integrated into the CdS framework. The observed overlap between Cd, S, and Nb indicates that doping has been successfully achieved. The presence of carbon from the green synthesis method indicates residual biomolecules that may have acted as reducing and stabilizing agents during the process.

3.3 Optical characteristics

The UV-Vis absorption graph (Figure 6) shows the absorbance spectra for CdS NPs and CdS-Nb counterparts (CdS-N1, CdS-N2, and CdS-N3). All samples exhibit a sharp absorption edge in the UV region, around 240–300 nm, which corresponds to the electronic transitions in the material. The doped samples (CdS-N1, CdS-N2, CdS-N3) show slightly altered absorption behavior compared to pure CdS. The intensity and position of the absorption edge change slightly with increasing doping concentration. The absorbance increases for doped samples compared to pure CdS, indicating enhanced light absorption properties, likely due to doping-induced defects (Ekpekpo *et al.* 2013). There is a gradual decrease in absorption beyond 400 nm, which is characteristic of CdS NPs with a relatively wide bandgap. The Nb ions may improve the separation of charge carriers (electrons and holes), leading to more effective light absorption and this may be the reason for the enhanced absorption. Furthermore, higher doping concentrations may introduce plasmonic behavior in Nb, further enhancing light interaction. To calculate the direct bandgap using the Tauc plot (Yu *et al.* 2019): where, α is the absorption coefficient, hν is the photon energy, Eg is the bandgap energy.

$$(\alpha h\upsilon)_n = A(h\nu - E_g) \quad (3)$$

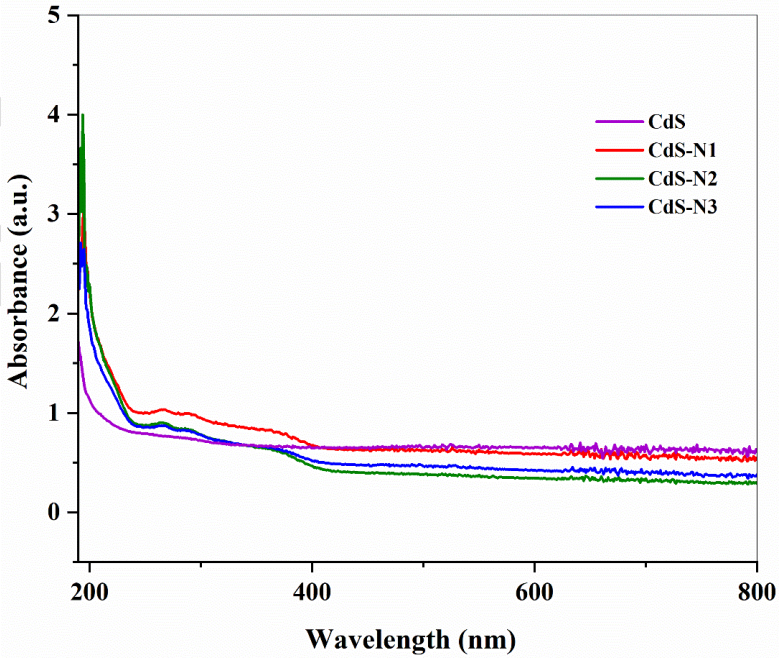

Figure 6. UV-visible analysis of synthesized NPs

The direct bandgap is estimated to be 2.41, 2.50, 2.60, and 2.46 eV, respectively for CdS NPs, CdS-N1, CdS-N2, and CdS-N3. The absorption edges of the doped samples shifted to higher energies with decreasing crystal size, consistent with the quantum confinement effect. Smaller NPs have a higher surface-to-volume ratio, leading to more surface states that can contribute to electronic transitions. CdS-N2 (15.4 nm) shows an increase in bandgap (~2.60 eV) because both quantum confinement and doping effects contribute significantly. Whereas, as the size decreases for higher concentrations (CdS-N3), lattice strain and defects become more significant, which can alter the electronic structure, leading to bandgap changes. The increase in bandgap was attributed to the quantum confinement effect and the introduction of donor levels near the conduction band, enhancing n-type conductivity (Yogamalar *et al.* 2015).

3.4 Visible-light-driven Photocatalytic Degradation activity

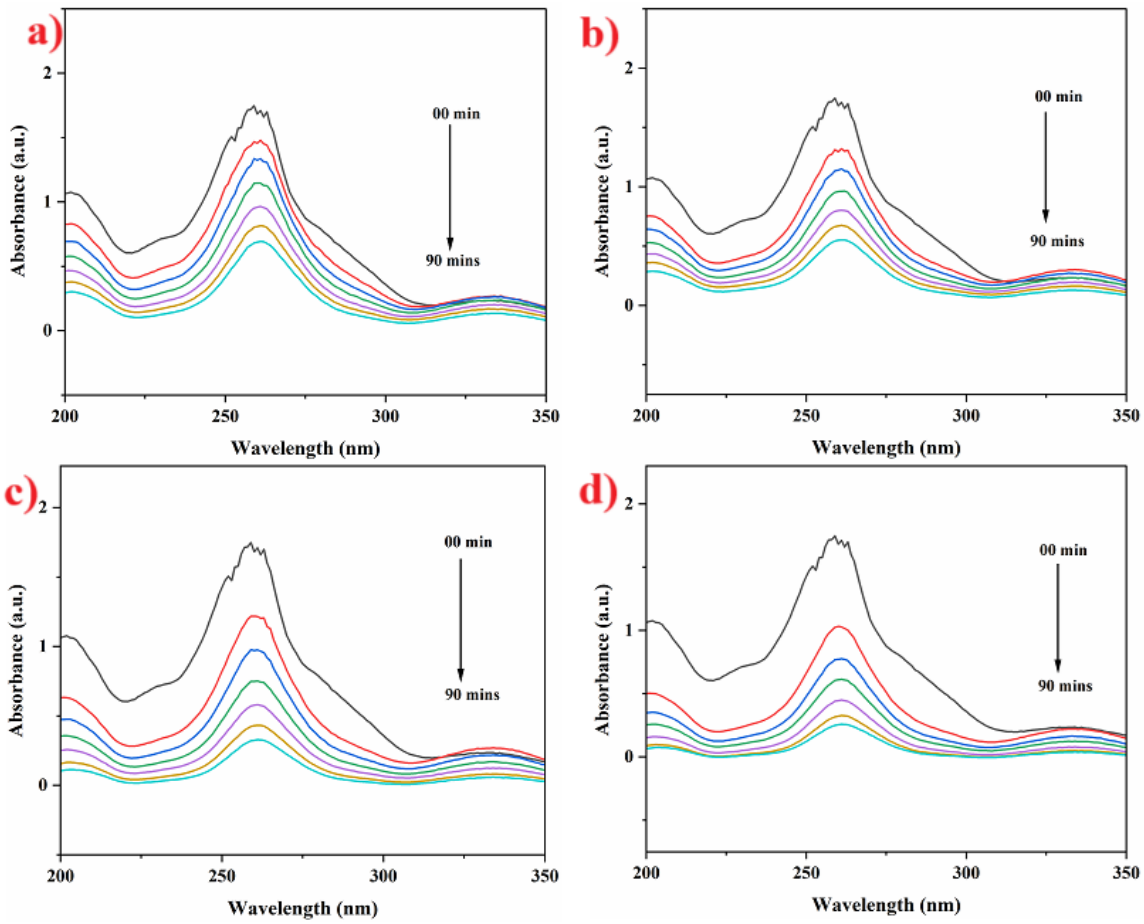

Figure 7. Time-dependent degradation graph for Alizarin red dye: (a) CdS, (b) CdS-N1, (c) CdS-N2, (d) CdS-N3

The photocatalytic and stability performance of undoped CdS and Nb-doped CdS (CdS-N1, CdS-N2, CdS-N3) with different Nb doping levels (1%, 2%, and 3%) for degrading two textile dyes, (anionic-Alizarin Red and cationic-Malachite Green**)** have been demonstrated under visible-light irradiation. Figure 7 and 8 demonstrates the time-dependent absorbance-dye degradation graph for Malachite green and Alizarin red dye. Therefore, the characteristic absorption peak of alizarin red (at 271 nm), and Malachite green dye (at 619 nm) decreases when irradiation time is extended from 0-90 mins by the influence of nano-catalysis. Figure 9

(a & b) illustrates the extent of dye degradation, represented by C/Co, as a function of sunlight irradiation time. In the absence of a catalyst, the C/Co values remain stable throughout the irradiation period. However, in the presence of a catalyst, the C/Co graph progressively decrease with increasing irradiation time. Figure 9 (c & d) presents the pseudo-first-order kinetic data curves, showing a linear relationship among the natural log of the concentration ratio (C/Co) and irradiation time and the photocatalytic process follows pseudo-first-order kinetics (Jain *et al.* 2021).

$$\ln\left(\frac{C}{Co}\right) = -kt \tag{4}$$

The equation articulates the correlation between the concentration of the dye at a specified time (C), the dye's initial concentration (Co), and the constant reaction rate (k).

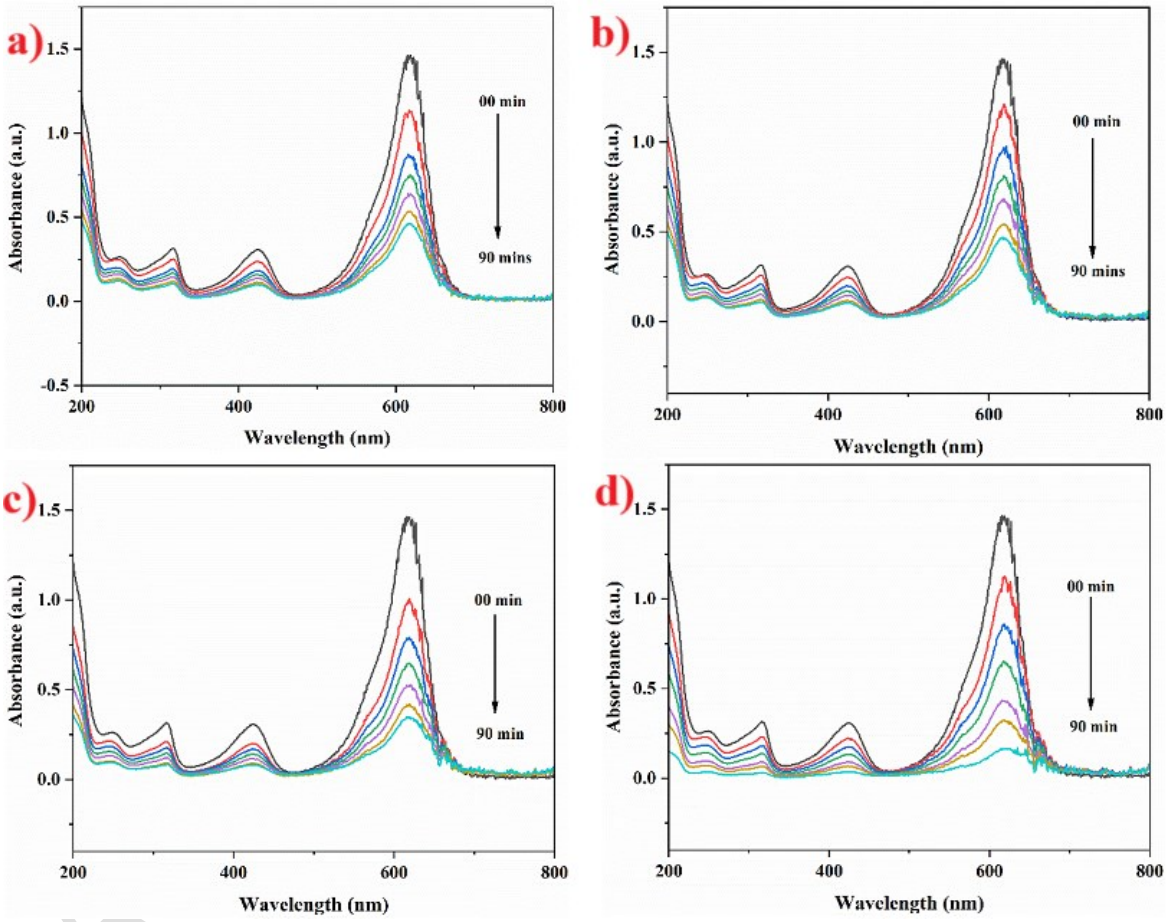

Figure 8. Time-dependent Absorbance-dye degradation graph for Malachite green dye: (a) CdS, (b) CdS-N1, (c) CdS-N2, (d) CdS-N3

The reaction rate constant for Alizarin red dye is determined to be 1.007, 1.21, 1.79, and 2.03 $x10^{-2}$ min^{-1} respectively for CdS, CdS-N1, CdS-N2, and CdS-N3. Moreover, for Malachite green dye is determined as 1.2, 1.27, 1.53 and 2.32 $x10^{-2}$ min^{-1} for CdS, CdS-N1, CdS-N2 and CdS-N3 respectively. At the end of irradiation, the maximum degradation percentage of Malachite green is 65.9, 69.4, 76.1, and 88.7% for CdS, CdS-N1, CdS-N2, and CdS-N3 respectively. Likewise, the maximum degradation of Alizarin red dye percentage is 59.5, 67.7, 80.8, and 84.9%, respectively for CdS, CdS-N1, CdS-N2, and CdS-N3.

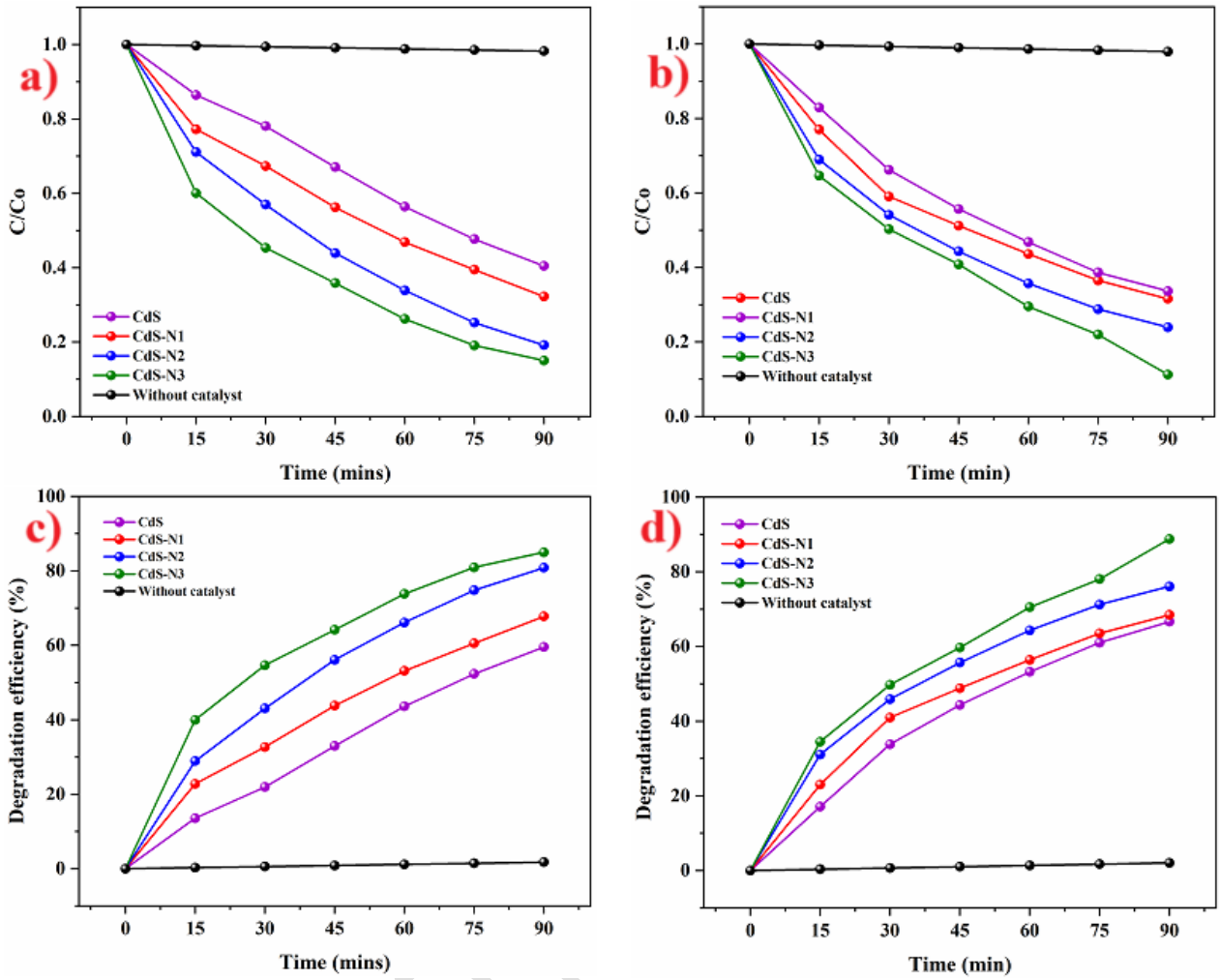

Figure 9. C/Co graph (a) and Degradation efficacy (c) graph for Alizarin red; C/Co graph (b) and Degradation efficiency (d) graph for Malachite green dye

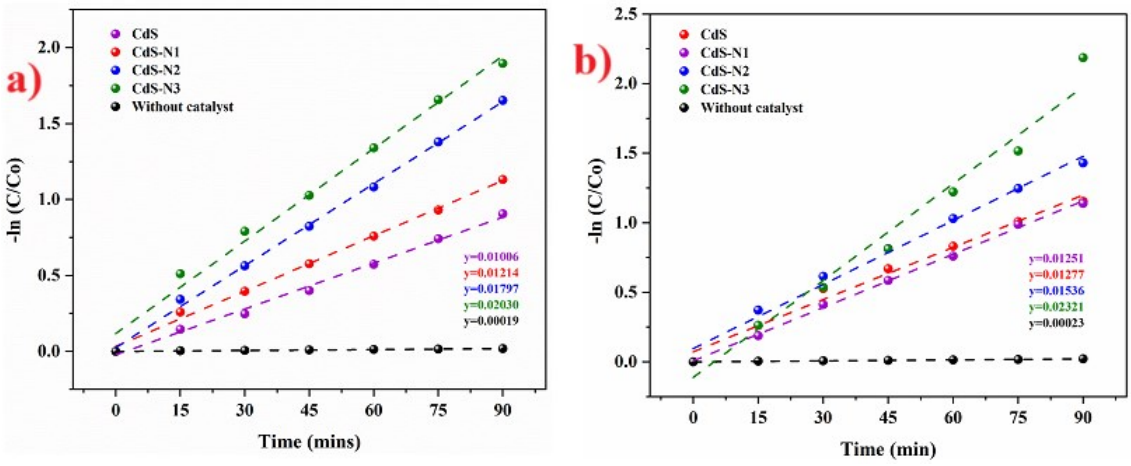

Figure 10. Pseudo-first-order kinetics graph for Alizarin red (a) and Malachite green (b) dye

Consequently, the analysis derived from UV-visible dye absorption spectra (Figure 7), the C/Co curve (Figure 8), and the pseudo-first-order kinetics (Figure 3) indicates that the cationic dye (Malachite green) exhibits a greater susceptibility to degradation compared to the anionic

dye (Alizarin red) when subjected to direct sunlight irradiation. This is because its positively charged molecular structure allows it to readily interact with the negatively charged electrons and reactive oxygen species (*OH and O_2^{*-}) generated on the surface of the CdS NPs (Yogamalar *et al.* 2015) where, malachite green has better adsorption on the surface of CdS NPs due to its structure and positive charge, which increases the interaction with active sites. Alizarin red dye adsorption is relatively weaker due to steric hindrance and lower affinity, reducing the availability of the dye for photocatalytic degradation. Moreover, phytochemical substances on the NP surface may function as a sensitizer, augmenting light absorption and facilitating effective charge separation, each of being essential for photocatalytic processes (Qusti *et al.* 2018). Figure 12 shows the bar graph for dye degradation efficiency, and the rate constant values are summarized in Table 2.

Table 2. Nanocatalyst with kinetic rate constant and degradation efficiency for 90 mins.

Sample	Dye used	Kinetic rate constant (x 10^{-2} min^{-1})	Degradation efficiency (%)	Stability efficiency after 5 cycles (%)
CdS	Alizarin red	1.007	59.52	54.5
CdS-N1		1.21	67.75	63.4
CdS-N2		1.79	80.83	74.9
CdS-N3		2.03	84.97	79.9
CdS	Malachite green	1.2	65.94	61.4
CdS-N1		1.27	69.42	64.4
CdS-N2		1.53	76.15	71.8
CdS-N3		2.32	88.76	84.1

In the photocatalytic degradation mechanism, when the CdS nano-catalyst is exposed to sunlight electrons are excited to the conduction band (CB) and holes are left behind in the valence band (VB) (Jain *et al.* 2021).

$$CdS + h\nu \rightarrow CdS\ (e^- + h^+) \quad (5)$$

This step initiates the photocatalytic process. Then, the photogenerated electron-hole pairs migrate to the surface of the CdS NPs. The Nb doping enhances charge separation by creating mid-bandgap states, reducing electron-hole recombination, and increasing catalytic efficiency. These photogenerated charge carriers participate in redox reactions to produce ROS, which play a critical role in dye degradation. At the conduction band (Reduction reactions), electrons (e_{CB}^-) interact with dissolved oxygen molecules (Yue *et al.* 2017).

$$e^- + O_2 \rightarrow O_2^- \text{ (Superoxide radical)} \quad (6)$$

$$O_2^- + H^+ \rightarrow HO_2 \text{ (Hydroperoxide radical)} \quad (7)$$

$$HO_2 + e^- + H^+ \rightarrow H_2O_2 \text{(Hydrogen peroxide)} \quad (8)$$

$$H_2O_2 + e^- \rightarrow OH^- + *OH \text{ (Hydroxyl radical)} \quad (9)$$

At the valence band (oxidation reactions), holes (h_{VB+}) react with hydroxide ions.

$$h^+ + H_2O \rightarrow H^+ + OH^* \quad (10)$$

$$OH^- + h^+ \rightarrow OH* \quad (11)$$

The generated reactive oxygen species and holes degrade the dye molecules via two main pathways. One by oxidative pathway and the other by radical pathway. The photogenerated holes (h^+) directly oxidize the dye molecules and ROS such as *OH and O_2^-* attack the dye molecules, breaking their bonds and leading to mineralization. The dye molecules are broken down into smaller, less toxic intermediates or completely mineralized into CO_2, H_2O, and inorganic ions. The catalytic degradation mechanism has been illustrated in Figure 11 (Oliveira *et al.* 2014).

$$\text{Dye molecules} + *HO + O_2- \rightarrow \text{Degraded products } (CO_2 + H_2O) \quad (12)$$

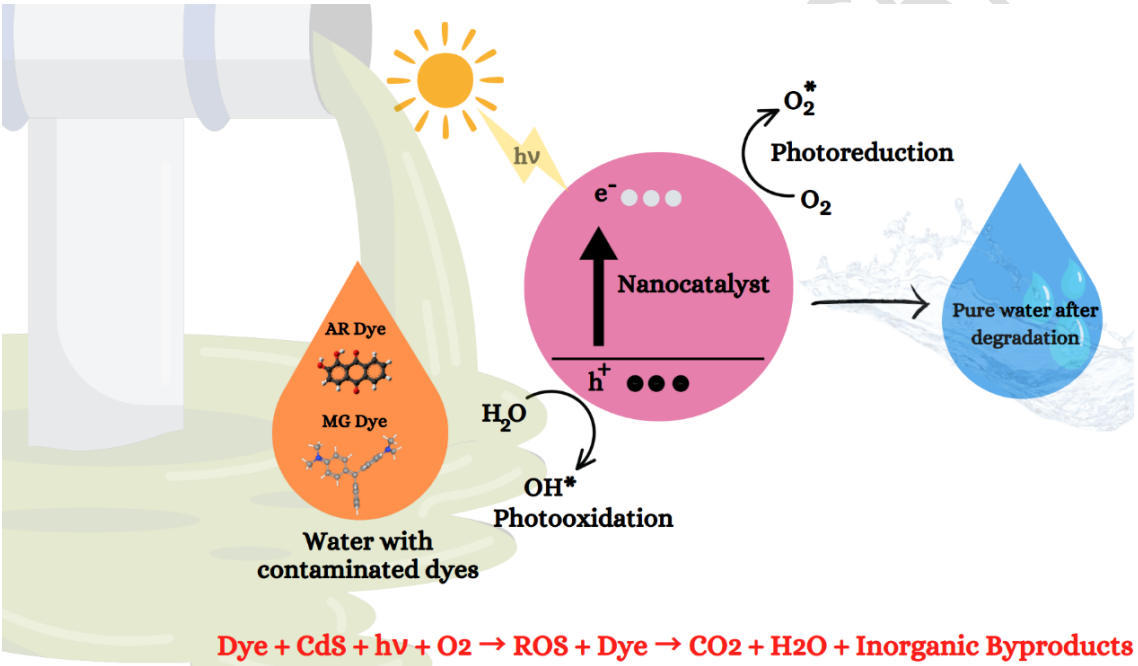

Figure 11. Degradation mechanism of prepared nanocatalyst

The examination of the photocatalyst's reusability and stability carries considerable economic significance. Consequently, this study sought to examine the stability of the photocatalyst and investigate the feasibility of reusing nano-catalysts, as illustrated in the bar graph presented in Figure 12 (b). Subsequent to each phase, the catalyst engaged in a systematic process of reconstitution, followed by washing and drying in an oven, thus facilitating its reusability. The experiment was carried out over a series of five distinct cycles. The degradation percentages of anionic alizarin red dye decreased from 59.5 % to 54.5 % for CdS NPs, 67.7 % to 63.4% for CdS-N1, 80.8 % to 74.9 % for CdS-N2 and 84.9 % to 79.9 % for CdS-N3 respectively and for cationic malachite green dye decreased from 65.9% to 61.4% for CdS NPs, 69.4 % to 64.4 % for CdS-N1, 76.1 % to 71.8 % for CdS-N2 and 88.7 % to 84.1 % for CdS-N3, respectively. Hence, it may be due to the organic layer from the extract can act as a photosensitizer, absorbing light and transferring energy to the CdS NPs. This improves light absorption in the visible

region, boosting the photocatalytic activity. Thus, the antioxidant properties of the extract components may also reduce oxidative stress on the NPs, enhancing their stability during repeated catalytic cycles and it revealed that a mere 5% underwent dissolution following five reuse cycles. Hence, owing to the minimal decrease in photocatalytic activity, this prepared nano-catalyst exhibits remarkable stability in photocatalytic activities.

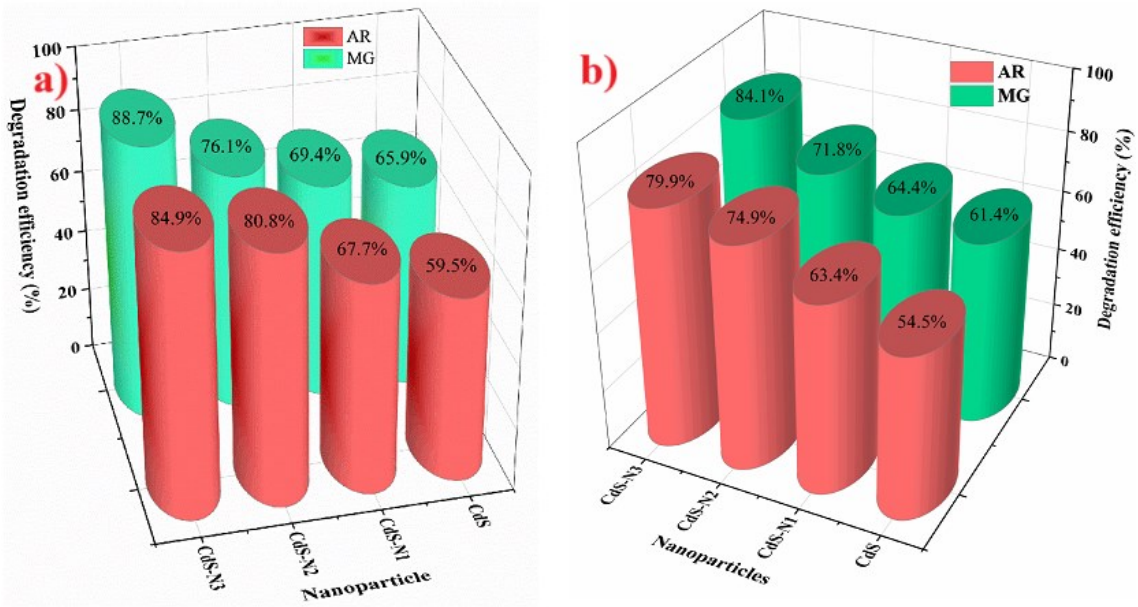

Figure 12. Degradation efficiency (a) and reusability efficiency after five cycles (b) of the synthesized CdS, and CdS-doped Nb particles

4. Antibacterial Activity

The antibacterial activity of CdS NPs and CdS-Nb at varying concentrations against bacterial strains, compared to the standard antibiotic Chlortetracycline (CT 30 µg), is presented in Table 3. The average diameter of bacterial growth inhibition zones, measured in mm and presented in bar graph Figure 14, reveals that higher NP concentrations demonstrate greater efficacy, particularly against Gram-positive bacteria compared to Gram-negative bacteria. For *S. aureus*, the zone of inhibition (ZOI) increases from 15 mm to 24 mm as the nanocatalyst concentration rises. Similarly, for *E. coli*, the ZOI grows from 11 mm at 25 µg/µl to 21 mm at 100 µg/µl. These findings confirm that CdS NPs are effective against both bacterial strains, with increased concentrations resulting in enhanced antibacterial activity (Dadmehr *et al.* 2022).

Table 3. Antibacterial activity of CdS NPs and CdS-Nb at different concentrations

Bacterial strain	**Zone of inhibition (mm)**															
	CdS				**CdS-N1 (µg/µl)**				**CdS-N2 (µg/µl)**				**CdS-N3 (µg/µl)**			
	Std	**25**	**50**	**100**	**Std**	**25**	**50**	**100**	**Std**	**25**	**50**	**100**	**Std**	**25**	**50**	**100**
S. aureus	15	17	20	21	15	17	18	22	16	18	21	23	17	20	23	24
E. coli	11	13	15	19	12	15	16	18	13	15	20	22	14	17	19	21

From table 3, it shows that CdS NPs and CdS-Nb exhibit a larger ZOI for Gram-positive compared to Gram-negative bacteria. This difference can be attributed to variations in the structural and chemical properties of the bacterial cell walls, which influence their interaction with NPs (Midya *et al.* 2019). The gram-positive bacteria cell wall is primarily composed of a thick layer of peptidoglycan, which is porous and allows NPs to penetrate more easily. This permeability facilitates direct contact between the NPs and the bacterial cell membrane, increasing oxidative stress and disrupting cellular functions. The CdS NPs generate ROS upon light exposure, which causes oxidative damage to bacterial cells. The ROS can more easily penetrate the simpler, more porous cell wall of Gram-positive bacteria. In Gram-negative bacteria, the outer membrane reduces the diffusion of ROS, diminishing their antibacterial effect. The peptidoglycan in positive bacteria contains teichoic acids, which carry a negative charge. This enhances electrostatic attraction among the NP and the bacterial surface, leading to better adherence and antibacterial activity. Whereas, the lipopolysaccharides layer in Gram-negative bacteria is more hydrophilic and less negatively charged, reducing NP adhesion and interaction (Dadmehr *et al.* 2022). The general bacterial mechanism has been illustrated in Figure 13.

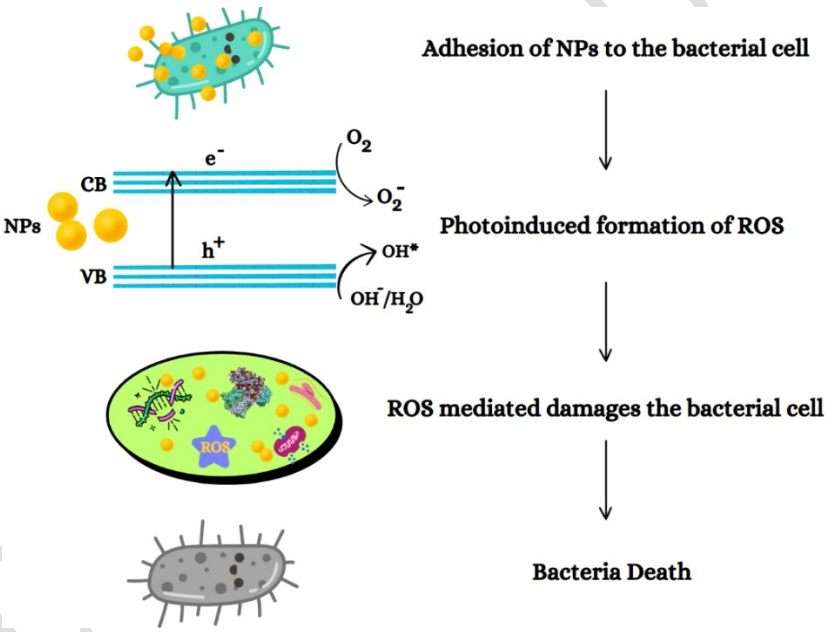

Figure 13. Graphic representation of the antibacterial mechanism

The CdS and CdS-Nb NPs directly interact with bacterial cells, disrupting the integrity of their membranes. Physical interactions between the NPs and the bacterial cell wall cause mechanical stress, leading to pore formation. ROS further weakens the membrane, causing the leakage of cytoplasmic contents and loss of cell viability. They further damage intracellular proteins and enzymes, disrupting metabolic activities. The Nb doping significantly enhances these effects by improving charge separation, increasing ROS generation, and facilitating stronger interaction with bacterial cells which makes CdS-Nb a more potent anti-bacterial agent compared to undoped CdS.

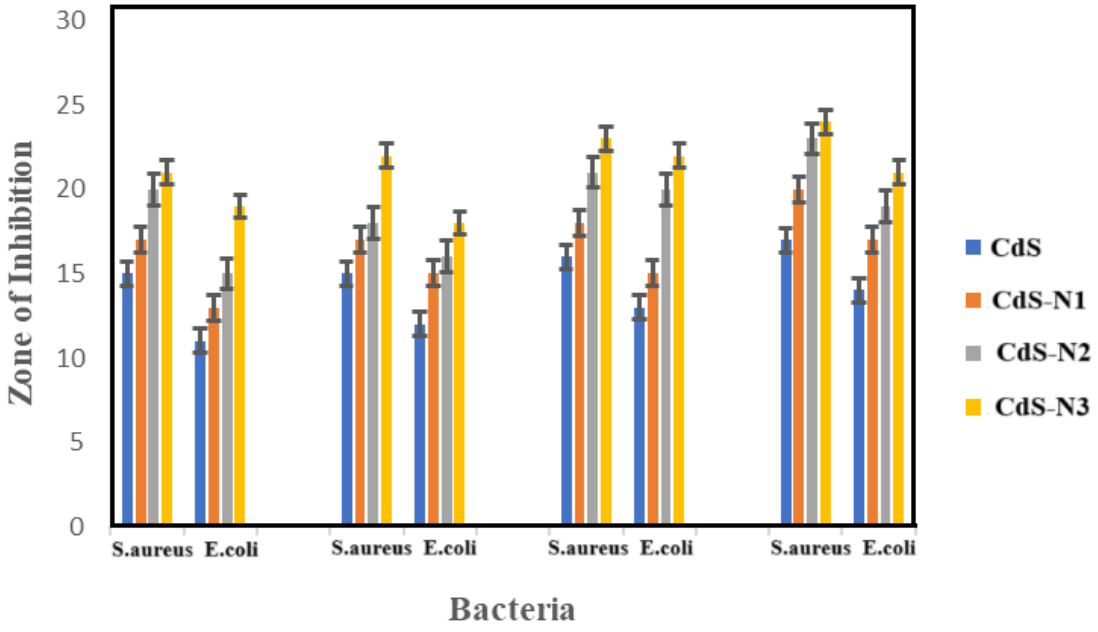

Figure 14. The antibacterial activity of synthesized NPs

5. Antioxidant behavior

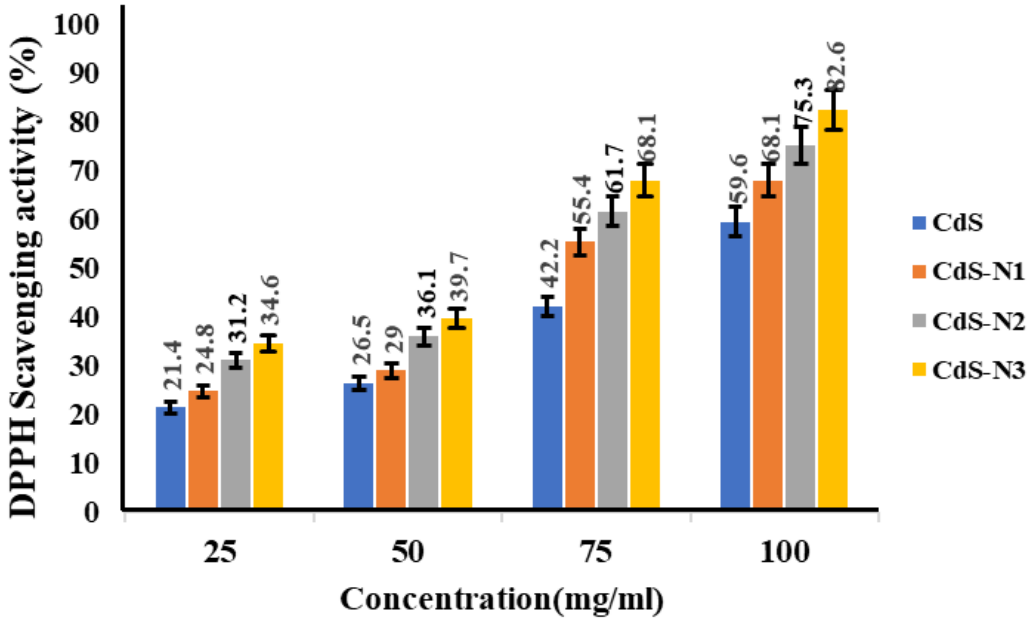

Figure 15. DPPH scavenging activity of synthesized NPs

The antioxidant potential of undoped CdS and Nb-doped CdS (CdS-N1, CdS-N2, CdS-N3) with different Nb doping levels (1%, 2%, and 3%) is investigated at dosage levels of 25, 50, 75, and 100 µg/µL, as illustrated in Figures 15. It is noted that with an increase in the concentration of NPs, their DPPH scavenging free radical activity significantly increases, as evident in the DPPH scavenging solution becoming transparent. At the highest concentration, the percentage of DPPH scavenging is found to be 83.4% for 100 mg/ml, respectively. At higher concentrations (CdS-N3), they generate more reactive sites for scavenging hydroxyl radicals, superoxide anions, and hydrogen peroxide. The NP may facilitate the conversion of

highly reactive ROS into less reactive or neutral species through electron transfer processes. Moreover, green extract bioactivity stabilizes the NP and directly participates in free radical scavenging.

6. Conclusion

In this study, green-synthesized Nb-doped CdS NPs were successfully prepared using *Syzygium cumini* seed extract as a reducing agent. The morphological tuning of the NPs was achieved by varying the Nb doping concentrations, resulting in distinct structural forms, such as uniform NPs, petal-shaped structures, and rod-like morphologies, which significantly influenced their photocatalytic and antibacterial performance. The XRD analyses confirmed the formation of the wurtzite hexagonal phase and highlighted the impact of Nb doping on particle size. UV-visible results revealed a significant shift in the absorption edge with decreasing crystal size. In contrast, the absorption edges of the doped samples shifted to higher energies with decreasing crystal size, consistent with the quantum confinement effect. Specifically, the CdS-N1 (19.09 nm) sample displayed a bandgap of 2.50 eV, the CdS-N2 (15.4 nm) sample showed a bandgap of 2.60 eV, and the CdS-N3 (21.5 nm) sample exhibited a bandgap of 2.46 eV. The photocatalytic degradation of textile dyes, including Alizarin Red and Malachite Green, demonstrated a marked improvement in efficiency with increasing Nb concentration. CdS-N3, with 3% Nb doping, exhibited the highest degradation rates and stability, maintaining 79.9% and 84.1% efficiency after five cycles for Alizarin Red and Malachite Green, respectively. This indicates the robustness and reusability of the NPs for environmental remediation applications. Additionally, the synthesized NPs exhibited significant antibacterial properties against gram-positive bacteria with the highest ZOI of 24 mm for 100 µg/µl (CdS-N3). Furthermore, higher concentrations (CdS-N3) exhibited a higher 82.6% scavenging efficiency. The results suggest that Nb doping plays a crucial role in enhancing the photocatalytic, antioxidant, and antibacterial activities of CdS NPs, thus offering a sustainable and efficient solution for the treatment of textile dye wastewater and microbial contamination and the green-synthesized Nb-doped CdS NPs as a promising material for various environmental applications.

References

Abd, J.A., Mohammed, W.M. and Al-Nafiey, A. (2021). CdS nanostructured thin films synthesized by pulsed laser deposition for solar cell technology, Key Engineering Materials, **882**, 155-164.

Abdel-Aty, A.M., Elsayed, A.M., Salah, H.A., Bassuiny, R.I. and Mohamed, S.A. (2021). Egyptian chia seeds (Salvia hispanica L.) during germination: Upgrading of phenolic profile, antioxidant, antibacterial properties and relevant enzymes activities, Food Science and Biotechnology, **30**, 723-734.

Adeyemi, J.O., Oriola, A.O., Onwudiwe, D.C. and Oyedeji, A.O. (2022). Plant extracts mediated metal-based nanoparticles: synthesis and biological applications, Biomolecules, **12**, 627-638.

Ali, R.F., Nazemi, A.H. and Gates, B.D. (2017). Surfactant controlled growth of niobium oxide nanorods, Crystal Growth & Design, **17(9)**, 4637-4646.

Cui, X., Yang, Z., Zhang, X., Liu, W., Zou, B. and Liao, W. (2022). Fabrication of novel heterojunction of (1D) Nb_2O_5 nanorod/(0D) CdS nanoparticles for efficient removal of U (VI) from water, Applied Surface Science, **599**, 154027.

Dadmehr, M., Korouzhdehi, B., Tavassoli, A. and Malekkiani, M. (2022). Photocatalytic activity of green synthesized cadmium sulfide quantum dots on the removal of RhB dye and its cytotoxicity and antibacterial studies, Nanotechnology, **33(39)**, 395101.

Dravie, E.E., Kortei, N.K., Essuman, E.K., Tettey, C.O., Boakye, A.A. and Hunkpe, G. (2020). Antioxidant, phytochemical and physicochemical properties of sesame seed (Sesamum indicum L). Scientific African, **8**, e00349.

Ekpekpo, A. and Akpojivi, L. (2013). Synthesis and characterization of CdS and CdSe quantum dots by uv-vis spectroscopy. Journal of Emerging Trends in Engineering and Applied Sciences, **4(2)**, 273-280.

Jain, K., Patel, A.S., Pardhi, V.P. and Flora, S.J.S. (2021). Nanotechnology in wastewater management: a new paradigm towards wastewater treatment, Molecules, **26(6)**, 1797.

Kong, X., Yu, F., Zhang, H., Lv, F., Wang, Y., Yin, L., Huang, J. and Feng, Q. (2022). Synthesis and study of morphology regulation, formation mechanism and photocatalytic performance of CdS, Applied Surface Science, **576**, 151817.

Midya, L., Patra, A.S., Banerjee, C., Panda, A.B. and Pal, S. (2019). Novel nanocomposite derived from ZnO/CdS QDs embedded crosslinked chitosan: An efficient photocatalyst and effective antibacterial agent, Journal of hazardous materials, **369**, 398-407.

Nasir, J.A., Rehman, Z., Shah, S.N.A., Khan, A., Butler, I.S. and Catlow, C.R.A. (2020). Recent developments and perspectives in CdS-based photocatalysts for water splitting, Journal of Materials Chemistry A, **8(40)**, 20752-20780.

Nunes, B.N., Lopes, O.F., Patrocinio, A.O.T. and Bahnemann, D.W. (2020). Recent advances in niobium-based materials for photocatalytic solar fuel production, Catalysts, **10(1)**, 126.

Oliveira, L.C., Oliveira, H.S., Mayrink, G., Mansur, H.S., Mansur, A.A. and Moreira, R.L. (2014). One-pot synthesis of CdS@ Nb2O5 core–shell nanostructures with enhanced photocatalytic activity, Applied Catalysis B: Environmental, **152**, 403-412.

Qusti, A.H., Malkhasian, A.Y. and Salam, M.A. (2018). Enhancement of CdS nanoparticles photocatalytic activity by Pt and In_2O_3 doping for the degradation of malachite green dye in water, Journal of Molecular Liquids, **255**, 364-369.

Shabaani, M., Rahaiee, S., Zare, M. and Jafari, S.M. (2020). Green synthesis of ZnO nanoparticles using loquat seed extract; Biological functions and photocatalytic degradation properties. Lwt, **134**, 110133.

Wang, W.N., Widiyastuti, W., Ogi, T., Lenggoro, I.W. and Okuyama, K. (2007). Correlations between crystallite/particle size and photoluminescence properties of submicrometer phosphors, Chemistry of Materials, **19(7)**, 1723-1730.

Yi, T.F., Sari, H.M.K., Li, X., Wang, F., Zhu, Y.R., Hu, J., Zhang, J. and Li, X. (2021). A review of niobium oxides based nanocomposites for lithium-ion batteries, sodium-ion batteries and supercapacitors, Nano Energy, **85**, 105955.

Yogamalar, N.R., Sadhanandam, K., Bose, A.C. and Jayavel, R. (2015). Quantum confined CdS inclusion in graphene oxide for improved electrical conductivity and facile charge transfer in hetero-junction solar cell, RSC advances, **5(22)**, 16856-16869.

Yu, H., Peng, Y., Yang, Y. and Li, Z.Y. (2019). Plasmon-enhanced light–matter interactions and applications, npj Computational Materials, **5(1)**, 45.

Yue, Z., Liu, A., Zhang, C., Huang, J., Zhu, M., Du, Y. and Yang, P. (2017). Noble-metal-free hetero-structural CdS/Nb_2O_5/N-doped-graphene ternary photocatalytic system as visible-light-driven photocatalyst for hydrogen evolution, Applied Catalysis B: Environmental, **201**, 202-210.